Polymer Testing 135 (2024) 108459

Contents lists available at ScienceDirect

Polymer Testing

journal homepage: www.elsevier.com/locate/polytest

Prediction and analysis of flexural stiffness for 3D-printed continuous fiber–reinforced composites with different matrix fill ratios and layer orders

Csenge Tóth [a,b], Ábris Dávid Virág [a], László Mihály Vas [a], Norbert Krisztián Kovács [a,b,*]

[a] Department of Polymer Engineering, Faculty of Mechanical Engineering, Budapest University of Technology and Economics, Műegyetem rkp. 3., H-1111, Budapest, Hungary
[b] MTA-BME Lendület Lightweight Polymer Composites Research Group, Műegyetem rkp. 3., H-1111, Budapest, Hungary

ARTICLE INFO

Keywords:
3D printing
Continuous fiber reinforcement
Classical laminate theory
Bending test
Thermoplastic composite

ABSTRACT

Bending load is often encountered in engineering applications, but it is less studied for 3D-printed continuous fibre–reinforced composites (CFRC). We present the flexural properties of 3D-printed composites as a function of layer order and matrix fill ratio. We applied Classic Laminate Theory to estimate the flexural modulus and showed that the Kerner-Hashin model is suitable for taking voids into account when calculating the elastic properties of the matrix layer. Using optical microscopic analysis, we identified the main defect sources of 3D-printed CFRC structures, such as voids, fibre waviness, fragmentation and poor bonding between laminas. By performing failure analysis based on the Fibre Bundle Cell method, we found that the use of top/bottom-type reinforcement instead of alternating layering will increase the reliability of the 3D-printed composites under bending load. Furthermore, the failure process will be more gradual and cover higher load levels, which increases safety.

1. Introduction

With the growing demand for customised industrial products, additive manufacturing of composites with a polymer matrix has made great progress in recent years [1–3]. This is mainly due to the increasing range of materials that can be used, and also the fact that 3D printing involves fewer steps to produce the final parts compared to traditional manufacturing processes. With the use of continuous reinforcing fibres, the mechanical properties of the product can be significantly improved, and high-performance parts can be produced with complex geometries [4–6]. Special path planning options also facilitate the design of shape morphing and self-monitoring lightweight structures [7].

To make 3D-printed composite parts suitable for certain applications, it is necessary to estimate the mechanical properties of the structure. Bending load often occurs in engineering applications, and the response of composites to these stresses is highly dependent on their structure. 3D-printed continuous fibre–reinforced composites (CFRCs) have a multi-level structure, with the smallest unit being a single printed bead, multiple printed beads forming a single layer, and multiple layers forming the laminate [8]. The structure is influenced by several manufacturing parameters such as the printing direction or the order of layers. Araya-Calvo et al. [9] investigated the effects of reinforcement pattern, reinforcement distribution, fibre orientation, and fibre content. The authors applied the design of experiments as a statistical method, and they determined a configuration that maximises flexural properties. Since methods based on large numbers of tests are often inefficient in terms of material use and cost, analytical and numerical methods are gaining ground to estimate the load-bearing of 3D-printed structures. Studies mostly focus on tensile load [10–14], calculations for flexural load are less common. Rajpurohit et al. [15] applied the Classical Laminate Theory (CLT) to predict flexural strength as a function of infill orientation, for neat polylactic acid (PLA) specimens. The authors found good agreement between the measured and estimated flexural strength. Torre and Brischetto [16] also reported that CLT-based calculations give reliable predictions for flexural properties, also for neat PLA specimens. The authors estimated the flexural modulus with a maximum error of 7.6 %. Somireddy and Czekanski [17] investigated short carbon fibre–reinforced 3D-printed composites. They reported that the CLT can predict flexural stiffness for thicker layers as well, but only for parts printed with flat build orientation.

The failure behaviour and the damage modes of 3D-printed CFRCs are less investigated under bending stress. In addition to laminates, 3D

* Corresponding author. Department of Polymer Engineering, Faculty of Mechanical Engineering, Budapest University of Technology and Economics, Műegyetem rkp. 3., H-1111, Budapest, Hungary.
E-mail address: kovacsn@pt.bme.hu (N.K. Kovács).

https://doi.org/10.1016/j.polymertesting.2024.108459
Received 22 January 2024; Received in revised form 12 April 2024; Accepted 17 May 2024
Available online 18 May 2024

printing also allows the manufacture of special composite structures, such as sandwich structures with lattice cores or hybrid composites with different fibre reinforcements. These show promising mechanical properties [18]. Li and Wang [19] designed sandwich structures with truss cores optimised for bending. The authors showed that the composites with truss cores exhibited the highest flexural strength and stiffness among the investigated specimens, and energy absorption can be also increased. Montazeri et al. [20] showed that the enhanced bending performance of auxetic structures is due to their special deformation, and it can be further increased with foam filling. Zahed et al. [21] found that flexural modulus and energy absorption increases with increasing the support thickness of honeycomb structures. Montazeri et al. [22] also found that hybrid lattice geometries can effectively increase the load-bearing capacity and energy absorption under bending load. Hybrid lattices, which are created by combining hexagonal and re-entrant unit cells, exhibit stiffness-changing and Poisson's ratio-changing behaviour [23]. Heterogeneous re-entrant honeycombs with designed geometric defects showed better stability and different buckling mode, which increased the energy absorption capability [24]. Regarding hybrid composites, Huang and Joosten [25] found that carbon and glass fibre hybrids show gradient (pseudo-ductile) failure under tensile load, which can promote safer applications. With the advent of multi-axis 3D printing, there are even more design possibilities for creating special composites. Shang et al. [26] prepared carbon fibre-reinforced PLA composites with out-of-plane fibre arrangement using a 7-axis 3D printing system. They reported increase in interlayer shear strength and flexural modulus, and the energy absorption capability was also improved.

Failure behaviour is typically analysed during the mechanical test with additional optical or acoustic analysis. Ma et al. [27] used acoustic emission and micro-computed tomography to investigate failure behaviour during 3-point bending and revealed the critical damage and delamination mechanisms. Hou et al. [28] analysed the failure process with a simulation model, in which the Hashin failure criterion was adopted. The proposed optimisation method and printing strategy improved the load-bearing capacity of the composites by 115 % compared to the reference. A less widespread, phenomenological method available for analysing the failure process is the so-called Fibre Bundle Cell (FBC) method. The FBC method was found to be suitable for analysing the failure of hybrid composites under tension [29] and unidirectional (UD) composites under flexural load [30,31].

In this paper, we present the analytical prediction of flexural modulus based on the Classical Laminate Theory (CLT) for different types of 3D-printed CFRCs. Three different layer orders were designed with three different matrix fill ratios, so a total of nine types of test specimens were investigated. Flexural properties were evaluated with 3-point bending and 4-point bending, which is rarely reported in the literature for 3D-printed composites. A phenomenological analysis of the experimental results was also carried out based on the FBC method, which provides a deeper understanding of failure.

2. Materials and methods

2.1. Specimen design

We designed three different of layer orders, and used three matrix fill rates for each. Polyamide (PA) matrix and carbon fibre (CF) reinforcement was used. The specimens consisted of two types of layers: matrix-only (PA lamina) and carbon fibre-reinforced layers (PA/CF lamina) (Fig. 1/a). The fibres were laid down in a concentric pattern (3 loops), thus creating UD composites with 0° fibre orientation. This configuration has the best flexural properties according to the literature [32,33].

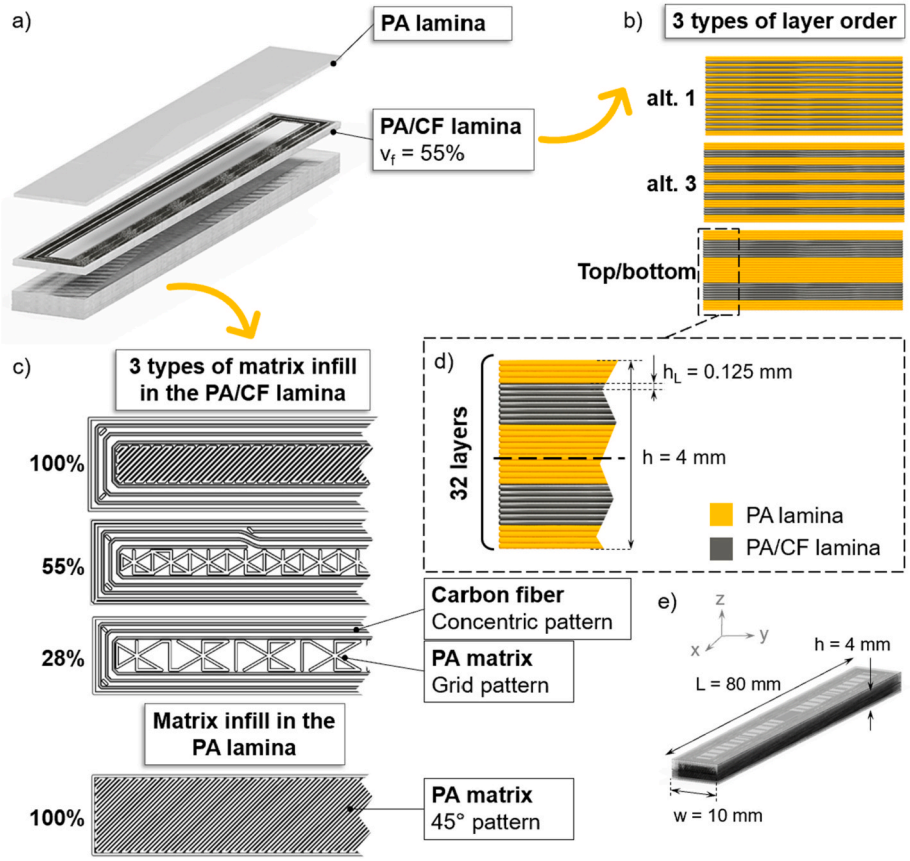

Fig. 1. Specimen design a) lamina types in the composites b) layer orders c) lamina types and the interpretation of the matrix fill ratio within a PA/CF lamina d) definition of layer height and e) geometry of the specimens.

The fill ratio of the matrix refers to the area between the contours of the reinforcing fibres (Fig. 1/c). At a fill ratio of 100 %, the matrix is deposited compactly at a 45° angle. At lower fill ratios (55 % and 28 %), the matrix is placed in a triangle grid pattern between the fibre contours. Triangular infill pattern can be preferable for bending load. Cojocaru et al. [34] showed that triangular infill has low variation in displacement, and Aloyaydi et al. [35] showed that it also has good energy absorption capabilities. However, as the infill density decreases (at 28 %) the spacing between Z-direction support elements increase, potentially weakening the structure. The fill rate of the PA laminas is always constant at 100 % (it is fixed in the slicing software). The layer orders were formed by stacking the PA and PA/CF layers in different sequences. Three types have been designed: the layers alternate one by one (alt. 1); triple alternating layers (alt. 3); the specimen has two thicker reinforced groups of layers placed in the upper and lower parts of the specimen in the bending configuration (Top/bottom). The layer orders are shown in Fig. 1/b. Each layer order is symmetrical and consists of 14 PA/CF laminas and 18 PA laminas. Sample height and layer height are fixed (Fig. 1/d). To investigate the effects of the amount of PA in the composites, we used 100 %, 55 %, and 28 % matrix fill ratios for each layer order. Thus, a total of 9 types of samples were printed. Table 1 shows the composition of each type.

Based on data from Eiger slicer software, the fibre content of the PA/CF lamina was 0.85 cm^3 in all cases. We also measured the fibre content in a lamina after extracting the fibres from the PA matrix manually. The fibre volume fraction (v_f), the matrix volume fraction (v_m), and the void volume fractions (v_v) were calculated with Eqs. (1)–(3), respectively. The fibre content determined by measurement and the fibre content determined from the slicing software (nominal) were 27 % and 26 %, respectively. The nominal values were used for further calculations.

$$v_f = \frac{V_f}{V_c} = \frac{\frac{m_f}{\rho_f}}{\frac{m_f}{\rho_f} + \frac{m_m}{\rho_m}} \tag{1}$$

$$v_m = \frac{(18 h_l w L) + \left((14 h_l w L) - V_f\right) r_m}{V_c} \tag{2}$$

$$v_v = 1 - v_f - v_m \tag{3}$$

where V_f is fibre volume, V_c is total volume, m_f and m_m are the mass of fibre and matrix, respectively. $\rho_f = 1.4$ g/cm^3 and $\rho_m = 1.1$ g/cm^3 are the densities of fibre and matrix, respectively [36]. In Eq. (2), h_l is the layer height, w is the width, L is the length of the specimen, and r_m is the matrix fill ratio. Specimen geometry is shown in Fig. 1/e.

2.2. Materials and 3D printing

The composites were manufactured with a Mark Two 3D printer from Markforged (USA). Specimen manufacturing is shown in Fig. 2. The Markforged printer features two nozzles on the print head, one for the matrix and one for the continuous fibre filament with a diameter of 1.75 mm and 0.35 mm, respectively (Fig. 2/b). The NylonWhite PA matrix and the PA/CF filament were supplied by Markforged. Zhang et al. [37] reported that the carbon fibres forming the PA/CF filament are coated with polyamide 6 (PA6) and are unevenly distributed in the filament. Due to incomplete impregnation, the PA/CF filament contains voids, and the average void content is 0.7 %. The PA6 coating provides good adhesion between the PA/CF filament and the PA matrix, however, porosity within the filament can lead to weak mechanical properties. The PA/CF filament consists of 1000 fibers, and the fibre volume content was calculated as 21.3–34.5 % [37–39].

We used the Eiger slicing software to prepare the models for 3D printing. The PA filament was kept in a dry-box during production to avoid moisture absorption. In one manufacturing cycle, 5 specimens per type were placed on the build platform with the wider sides flat.

Table 1
Matrix, fibre, and void volume fractions of the specimens (nominal values used in further calculations).

		100 %	55 %	28 %
Matrix fill ratio	r_m (−)	1	0.55	0.28
Matrix volume fraction	v_m (−)	0.74	0.66	0.61
Fibre volume fraction	v_f (−)	0.26	0.26	0.26
Void volume fraction	v_v (−)	0.00	0.08	0.13

2.3. Analytical methods

We applied the Classical Laminate Theory (CLT) to predict the bending stiffness for all laminates. Equivalent layer theories treat a heterogeneous laminate as a mechanically equivalent single layer with complex constitutive behaviour, thus reducing the 3D continuum problem to a 2D problem. The elastic properties of the PA and the PA/CF laminas were determined (Table 2 – detailed calculation is shown in the Appendix). In the case of the specimens with 55 % and 28 % matrix fill ratio, the effects of voids on the elastic properties were calculated with the Kerner-Hashin model [40]. Using Eq. (4), we calculated the effective tensile modulus of the matrix with void content (E_{me}). Then, we calculated the effective tensile modulus of the PA/CF laminas ($E_{PA/CF}$) with the Rule of Mixtures (Eq. (7)).

$$E_{me} = \frac{9 K_{me} G_{me}}{3 K_{me} + G_{me}} \tag{4}$$

where G_{me} is the effective shear modulus and K_{me} is the effective bulk modulus, given by Eqs. (5) and (6).

$$G_{me} = G_m \frac{(7 - 5\nu_m)(1 - V_v)}{(7 - 5\nu_m) + (8 - 10\nu_m) V_v} \tag{5}$$

$$K_{me} = \frac{4 G_m K_m (1 - V_v)}{4 G_m + 3 V_v K_m} \tag{6}$$

where $G_m = 0.8$ GPa is the calculated shear modulus of the matrix, $K_m = 1.7$ GPa is the bulk modulus provided by the Markforged NylonWhite datasheet, V_v is the calculated void volume content and $\nu_m = 0.39$ (−) is the Poisson's ratio of the matrix [41]. The effective tensile modulus was calculated as:

$$E_{PA/CF} = \nu_m E_{me} + v_f E_{CF} \tag{7}$$

where E_{me} is the effective matrix modulus and E_{CF} is the modulus of the carbon fibres.

We characterised the accuracy of the modulus predictions with the error given by Eq. (8).

$$\frac{\left|X_{CLT} - \left(X_{m,avg} + X_{m,SD}\right)\right|}{X_{CLT}} \le \delta\,(\%) \le \frac{\left|X_{CLT} - \left(X_{m,avg} - X_{m,SD}\right)\right|}{X_{CLT}} \tag{8}$$

where X stands for strength or modulus, CLT, "m,avg" and "m,SD" are subscripts for the calculated strength and modulus using the CLT method and the measured means and standard deviations, respectively.

Phenomenological analysis of the experimental results was performed with the Fibre Bundle Cell (FBC) method [31]. FBC is a decomposing and curve-fitting method based on iteration, which can be used to approximate the curves resulting from simple mechanical tests (e.g. flexural or tensile tests) with a closed formula, allowing the treatment of curves obtained from mechanical tests as functions. The formulas can be used for the analysis and comparison of measurement results and can be used in simulation software. The FBC is, in principle, a set of mechanical elements with predefined properties called fibre bundle cells, which can be connected in series and/or in parallel to build a network. For the fitting, we used E-bundles with linear mechanical characteristics in parallel connection. The stress-strain curve of each

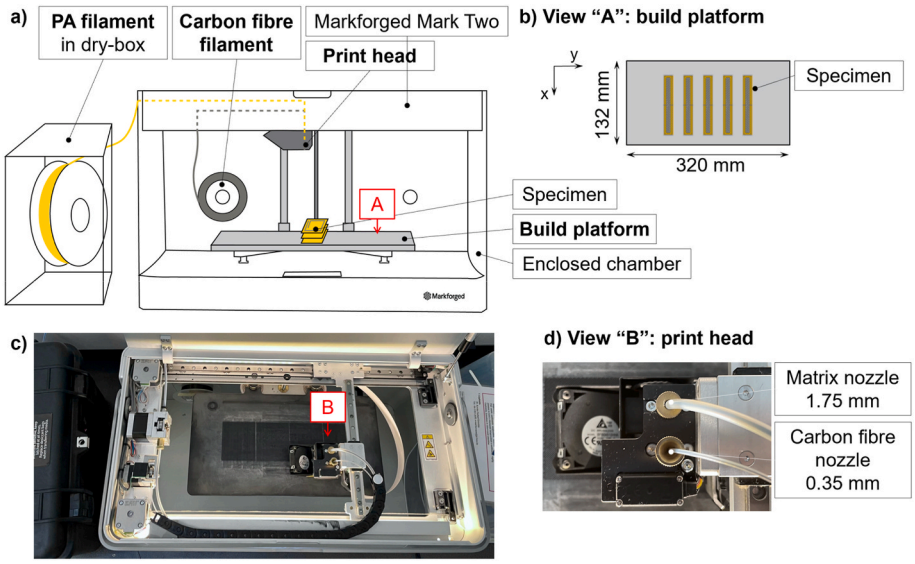

Fig. 2. Specimen production a) schematics of the 3D printing setup, b) arrangement of specimens on the build platform (top view), c) Markforged Mark Two 3D printer (top view), d) print head featuring two nozzles (top view).

Table 2
Calculated lamina properties.

Elastic properties		PA lamina	PA/CF lamina		
		100 %	100 %	55 %	28 %
Effective modulus of the matrix	E_{me} (GPa)	1.7	1.7	0.91	0.42
Effective modulus with carbon fibres	E_1 (GPa)	–	51.3	26.6	26.2
Transverse modulus	E_2 (GPa)	1.5	45.5	23.6	23.3
Shear modulus	G (GPa)	0.8	24.4	12.7	12.5

E-bundle ($\sigma_{E\text{-bundle}}(\varepsilon)$) can be obtained as the product of two curves (Eq. (9)):

$$\sigma_{E-bundle}(\varepsilon) = k(\varepsilon)\mathrm{R}(\varepsilon) \tag{9}$$

where ε is the strain of the bundle, k(ε) is the mechanical characteristic function, which describes the intact (damage-free) operation, and R(ε) is the reliability function, which is a complementary cumulative distribution function that describes the expected failure process. This simple multiplication-based treatment gives information about the failure behaviour with the use of the reliability function.

In this paper, we used Eq. (10) and Eq. (11) for the mechanical characteristic curve and reliability function, respectively:

$$k(\varepsilon) = c\varepsilon \tag{10}$$

where c (MPa) is a fitted stiffness parameter, and

$$R(\varepsilon) = 1 - Q_{\varepsilon_B}(\varepsilon) = 1 - \int_{-\infty}^{\varepsilon} \frac{1}{\sqrt{2\pi}D} e^{-\frac{(t-M)^2}{2D^2}} dt \tag{11}$$

where Q_{ε_B} is the normal distribution function of the strain at break of the bundle (ε_B), and M (−) and D (−) are the mean and standard deviation of ε_B, respectively.

A curve from a mechanical test can be very complex (e.g. containing many local maximum points). Therefore, using multiple bundles connected in parallel is recommended for greater accuracy. The number of bundles and the desired accuracy can be chosen arbitrarily. In this case, the approximating stress–strain curve is constructed as the sum of weighted stress–strain curves of multiple fibre bundles (Eq. (12)–(14)):

$$\sigma_{measured}(\varepsilon) \approx \sigma_{model}(\varepsilon) = k_{\sum}(\varepsilon)R_{\sum}(\varepsilon) \tag{12}$$

$$k_{\sum}(\varepsilon) = \sum_{i=1}^{n} p_i c_i \varepsilon = c\varepsilon \tag{13}$$

$$R_{\sum}(\varepsilon) = \sum_{i=1}^{n} p_i R_i(\varepsilon) = \sum_{i=1}^{n} p_i \left(1 - \int_{-\infty}^{\varepsilon} \frac{1}{\sqrt{2\pi}D_i} e^{-\frac{(t-M_i)^2}{2D_i^2}} dt\right) \tag{14}$$

where $k_{\sum}(\varepsilon)$ is the total mechanical characteristic curve, $R_{\sum}(\varepsilon)$ is the total reliability function and p_i is the weight of the ith model component (i = 1, …,n). In this case, we defined the weight of the ith model component as $p_i = c_i / \sum_{i=1}^{n} c_i$ (therefore $\sum_{i=1}^{n} p_i = 1$).

We used the reliability functions for further analysis. We performed the FBC method for each test to approximate the stress–strain curves using Microsoft Excel. In each case, we used a sufficient number of bundles (1–3) that allowed the accurately handling of the relevant sections of the curves. The fitting parameters (c_i, M_i, D_i) were optimised by iteration. The iteration was run until the normalised root mean squared error (NRMSE, Eq. (15)) was less than 5 %. The total reliability function of each flexural test was obtained as a result of the FBC method.

$$NRMSE = \frac{\sqrt{\frac{1}{N}\sum_{j=1}^{N}\left(\sigma_{measured}(\varepsilon_j) - \sigma_{model}(\varepsilon_j)\right)^2}}{\max_{1\le j\le N}\sigma_{measured}(\varepsilon_j)} \tag{15}$$

Fig. 3/a shows an approximation of a flexural curve with three E-bundles. This method is very useful for describing the measured flexural curve. In this case, the NRMSE was 3.4 %. Based on the FBC method, the resulting approximation curve can be interpreted as the product of two curves: the total mechanical characteristic function ($k_{\sum}$) and the total reliability function ($R_{\sum}$) (Fig. 3/b). The resulting $R_{\sum}$ was used to compare and analyse the failure processes.

2.4. Flexural tests

As part of the study, a comparison was made between the mechanical properties acquired from 3-point bending (3 PB) and 4-point bending (4 PB). We performed both tests on the specimens prepared with a 100 %

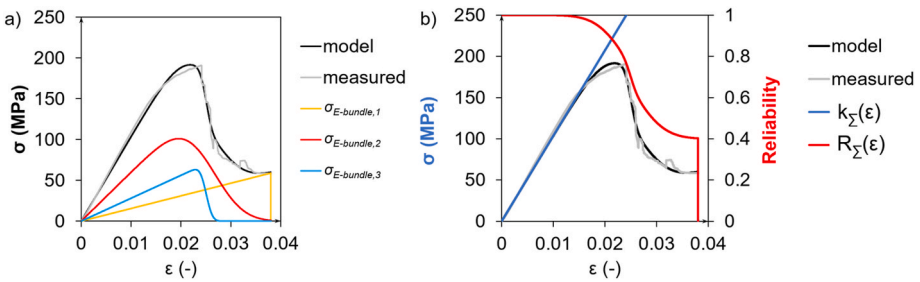

Fig. 3. a) Approximation of the tensile curve with three E-bundles, b) Flexural curve as the product of the total mechanical characteristic and the total reliability function.

matrix fill ratio, for all layer orders. In all other cases, 3-point bending was used. 3-point bending tests were carried out on a Zwick Z005 universal testing machine (Germany) (Fig. 4/a) according to EN ISO 14125 using a Zwick 3-point flexure test kit (Fig. 4/b) and a 5 kN load cell with a resolution of 0.1 N. 4-point bending tests were carried out on a Zwick Z020 universal testing machine (Germany) according to EN ISO 14125 using a Zwick 4-point flexure test kit (Fig. 4/c) and a 20 kN load cell with a resolution of 0.1 N. The cross-head speed was 10 mm/min for all tests, and 5 specimens were tested in each case. Fig. 4/d-e shows the testing arrangements and the moment distributions in case of 3 PB and 4 PB.

2.5. Measuring void content

The specimens were cut in half with a circular saw in the direction perpendicular to their length, and the resulting samples were embedded in epoxy resin. The cross-sections were polished with a LaboPol-5 polisher from Struers (Denmark) with a multi-fine grinding wheel and water cooling. Images of the surfaces were produced with a VHX-5000 optical microscope from Keyence Corporation (Belgium). The voids were identified by colour segmentation in the Keyence software, and the void fraction per cross-section was measured.

3. Results and discussion

3.1. CLT-based modelling and flexural test results

The results of the 3 PB and the 4 PB tests and the predicted modulus values can be seen in Fig. 5. Flexural strength is plotted as a function of matrix fill ratio (Fig. 5/a), and the three types of layer orders (alt. 1, alt. 3, and top/bottom) are also distinguished. Flexural strength increased slightly with increasing matrix infill rate. However, there was no significant difference between the 28 % and 55 % rates. In the case of the 100 % matrix fill ratio, flexural strength is the highest for the top/bottom layer order. This is expected since in this type of specimen, the reinforcement is placed where the load is highest.

In the case of the specimens with 55 % and 28 % matrix fill ratios, there is no significant change in strength as a function of layer order. For the 100 % fill ratio, we performed 4-point bending tests (4 PB) as well. The flexural strength and moduli were 40 % higher on average than those measured with 3 PB. This can be due to the distribution of bending moment along the length of the specimen, and the additional compressive and shear stresses that occur with 3 PB.

Experimental and predicted flexural moduli are shown in Fig. 5/b. For the 100 % matrix fill ratio, the highest modulus was obtained with the top/bottom and the lowest with the alt. 1 type. In the case of the samples with lower matrix fill ratios, the flexural modulus was also the highest for the top/bottom layer order. As with strength, there was no

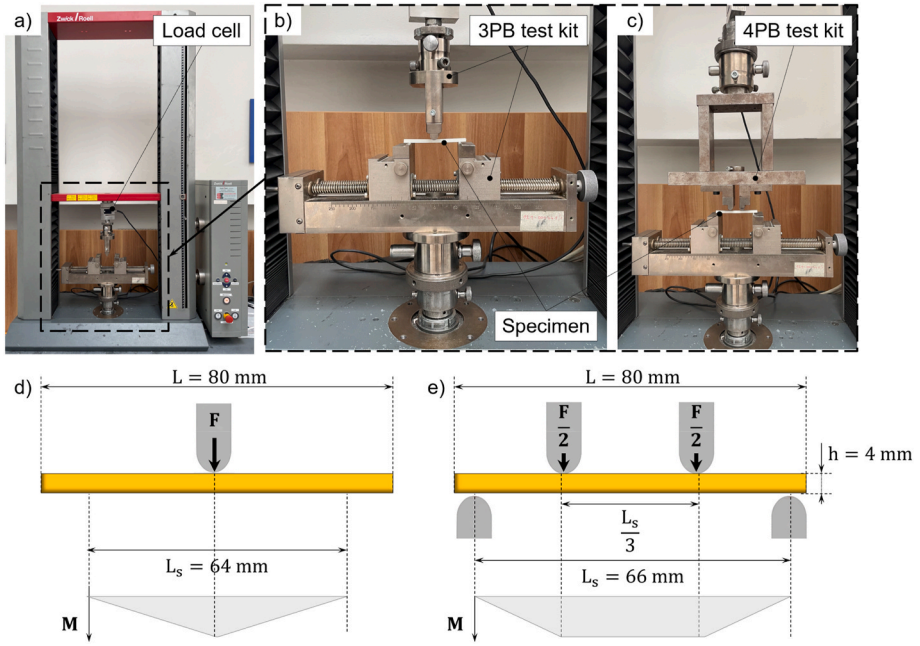

Fig. 4. a) test setup, b) 3-point bending (3 PB), c) 4-point bending (4 PB) test arrangement; moment distribution in case of the d) 3 PB and e) 4 PB tests. F and M denote the applied force and the generated bending moment, respectively.

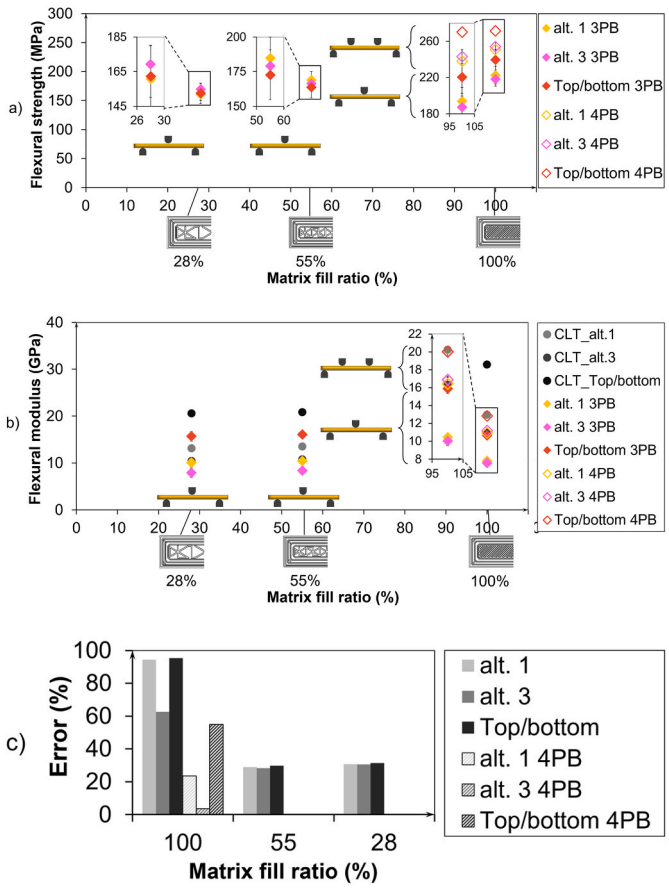

Fig. 5. Flexural test results obtained with 3-point bending and 4-point bending a) flexural strength and b) flexural modulus as a function of matrix fill ratio; c) calculated error (δ) between predicted and the measured moduli.

significant difference in modulus between the fill ratios of 28 % and 55 %. This means that the same mechanical properties can be achieved with less matrix material, thus reducing weight and costs, which is of great importance in engineering applications.

Fig. 5/c shows the error between the estimated and the measured flexural moduli. For the 100 % fill ratio, a compact, void-free structure was assumed for the calculations. In the case of the specimens with 55 % and 28 % matrix fill ratios, we calculated the elastic properties of the PA laminas that contain voids using the Kerner-Hashin model. It should be noted that these voids are controlled by the fill ratio and are not due to defects. The error averages 63–95 % when compared to the 3 PB test results, and 4–55 % compared to the 4 PB test results. This is because during 4 PB tests, the stress distribution is more homogeneous along the length of the specimen and fewer additional stresses occur, so the stress state is closer to pure bending. For the sample types with a reduced matrix fill ratio, the error ranges from 28 to 31 %, and for the 100 % matrix fill ratio, it is 63–95 % (all compared to 3 PB test results). This shows that the Kerner-Hashin model is suitable to take voids into account when the elastic properties of the matrix layer are calculated. Overall, the CLT-based methods presented are only suitable as a rough approximation due to the high error rates.

3.2. Phenomenology-based analysis

We carried out a phenomenological analysis to compare the damage processes. Our goal was to identify differences between the layer orders and demonstrate the differences between the 3 PB and the 4 PB tests. The analysis was performed for the 100 % matrix fill ratio based on the FBC method. Fig. 6/a and Fig. 6/c shows the reliability functions obtained with the use of the curve-fitting method described in Section 2.3. The reliability functions show the probability that ultimate failure will occur above the given strain. Using this statistical data, we plotted the failure probabilities as a colour map on the experimental curves.

The colour maps show the probability of failure of the composites under bending load (Fig. 6/b and d). In 3 PB results, the 50 % probability of failure for the alt.1 type occurs at an elongation of 0.025, while for the top/bottom type it occurs at an elongation of 0.035 on average. In the case of the 4 PB results, a similar trend can be noticed. Samples fail sooner if the layer order is more homogeneous (alt. 1 type). A more gradual failure process can be seen for the top/bottom type, which is preferable for the safe operation of composite structures [42].

Also, the reliability functions of the 3 PB results show a larger variance, while the reliability functions from 4 PB show a similar nature and a smaller variance. This is because during 3 PB tests, compressive and shear stresses are applied in addition to bending, while during 4 PB tests the stress is closer to pure bending. The additional stresses in 3 PB can cause multiple damage processes in the composites, leading to premature failure.

3.3. Meeting assumptions and sources of error

While the CLT is a useful tool for rough estimation for conventional composites, it is not yet widespread for 3D-printed composites. Defects resulting from 3D printing, such as improper interlayer bonding or the presence of voids, reduce the performance of the composites, which is generally not taken into account when using the CLT. The specific geometric features of 3D printed structures, such as grid infill or free fibre laying direction, present additional difficulties. In this section, we identify the sources of defects and examine how the boundary conditions of the classical plate theory are fulfilled. When applying the CLT, we assume that the composite consists of linear-elastic, orthotropic and quasi-homogeneous laminas, which are perfectly bonded together. Lamina thickness is assumed to be much smaller than its width and the length, and constant throughout the laminate. It is also assumed that the structure fulfils the Kirchhoff hypothesis [43].

The thickness of the composites presented in this study is of the same order of magnitude as the width, so they are not shell elements. However, the special structures that 3D printing can produce (e.g. sandwiches with grid cores) cannot be effectively exploited for thin composites. For thicker samples, CLT has been used successfully in some studies. Mishra and S.P [44]. predicted the in-plane tensile stiffness of 3D-printed structures of significant thickness (4 mm thickness, 6 mm width) with good agreement. Meng et al. [45] showed that the basic principles of CLT can be extended to 3 dimensions and can give reasonable results for flexural properties prediction. However, in order to apply predictive models to 3D printed composites, the sources of errors and the limits of applicability need to be explored.

Fig. 7 shows the main defect sources we identified for the 3D-printed composites. We measured the void content for the 100 % matrix fill ratio on the polished cross-section (Fig. 7/d). The voids are mainly located between the reinforcing fibres and at the interface of the reinforced and matrix-only laminas. Void content was independent of layer order, it was approximately 8 % in all cases. Voids can promote crack propagation and can cause delamination and premature failure, thus weakening the composite. We also measured lamina thickness (Fig. 7/e). The laminas are on average thinner than nominal layer thickness ($h_{L,nom}$ = 0.125 mm), which may be due to the pressure exerted by the extruder head during deposition. The weight of the stacked layers can further compress the lower layers. The relatively large deviation of the results shows that lamina thickness is not constant, but we found no trend as a function of layer order or sample height. Fibre defects can further reduce the performance of the composite. Fig. 7/c shows the optical microscopy image of a PA/CF layer, in which the CF bundle is wavy in some areas and also fragmented, especially in the corners. Shiratori et al. [46] also examined the folding mechanism and fibre breakage. Finally, we also

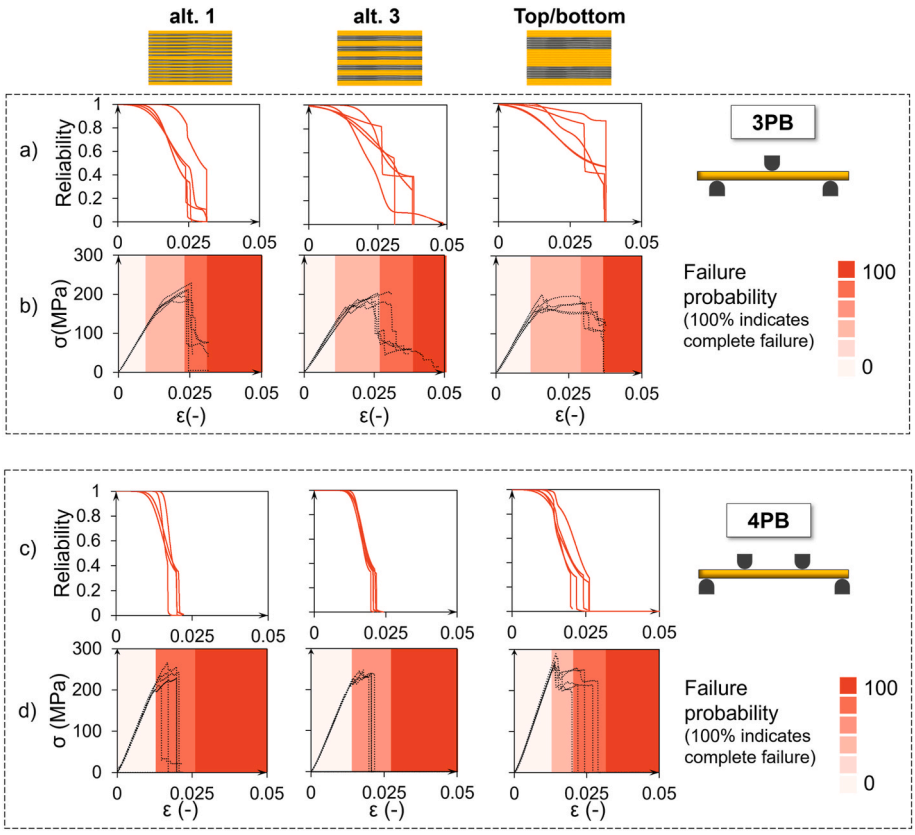

Fig. 6. Phenomenological analysis of the experimental results obtained with 3-point bending and 4-point bending for the 100 % matrix fill ratio, based on the FBC method a) and d) show the reliability functions, b) and d) show the failure probability colour maps. (For interpretation of the references to colour in this figure legend, the reader is referred to the Web version of this article.)

reviewed the literature to verify the assumption of bonding between laminas, as such tests are outside the scope of this research. It is reported that interlaminar properties are often weaker than longitudinal properties. The bonding between the laminas is strongly affected by the aforementioned 3D printing defects and manufacturing settings [47,48].

We conducted an analytical parametric study to investigate the effects of defect voids. The defect voids have irregular shapes and different sizes. These voids are mainly located within and between the PA/CF filaments, and between the PA matrix and the PA/CF filaments (Fig. 7). If there is no connection between the fibre and the matrix, load transfer is not effective. Thus, we assumed that fibres surrounded by or adjacent to voids do not fully participate in load transfer. To consider this negative effect in the CLT-based flexural modulus predictions, we defined the effective fibre content as follows. We assume that the void content is the same in all cross-sections and that the voids have a circular shape with a d_{void} diameter. We also assume that the fibres are tightly wrapped around the voids (Fig. 8/a). In this case, the number of voids (N_{void}) in a representative cross-section (A_{total}) is given as:

$$N_{void} = \frac{A_{total}}{A_{void}} = \frac{A_{total}}{\frac{d_{void}^2 \pi}{4}} \tag{16}$$

Based on Fig. 8/a the number of fibres surrounding a void ($N_{fiber,sur}$) can be determined using the radius of the fibre (r_{fibre}) and the radius of the void (R_{void}) (Eq. (17)):

$$N_{fibre,sur} = \frac{2\pi}{2\varphi} = \frac{\pi}{\sin^{-1}\left(\frac{r_{fibre}}{r_{fibre}+R_{void}}\right)} = \frac{\pi}{\sin^{-1}\left(\frac{d_{fibre}}{d_{fibre}+d_{void}}\right)} \tag{17}$$

where angle φ depends on the diameters of both the fibres and the voids.

Then, the effective fibre content ($v_{f,eff}$), which is the amount of fibre that is assumed to be fully attached to the matrix, can be given by Eq. (18).

$$v_{f.eff} = v_f \frac{N_{void} N_{fibre.sur}}{N_{fibre.total}} \tag{18}$$

where v_f is the total fibre content in a single reinforced lamina.

Eq. (16)–(18) shows that $v_{f,eff}$ depends only on the number of fibres adjacent to voids. To estimate the effect of the voids on the flexural modulus, we calculated the lamina properties using the effective fibre content as a parameter. Results can be seen in Fig. 8/b. The parametric study shows that, as expected, the more fibres connected to the matrix, the higher the flexural modulus. Voids (as defects) are common in 3D printed composites and affect the expected mechanical properties negatively. With the estimation method proposed in this study, the modulus predictions can be corrected, and the effect of inappropriate fibre-matrix adhesion can be taken into account.

4. Conclusion

This research focuses on the flexural properties of 3D-printed continuous fibre–reinforced composites. Specimens were prepared with a polyamide (PA) matrix and continuous carbon fibre (CF) reinforcement with three types of layer orders and three matrix fill ratios (28 %, 55 %, 100 %). We conducted 3-point bending (3 PB) and 4-point bending (4 PB) tests, and evaluated flexural properties as a function of the matrix fill ratio and layer order. We obtained the highest strength and modulus with the top/bottom layer order. The flexural strength and moduli measured with 4 PB were on average 40 % higher than those measured with 3 PB, due to the distribution of bending moment along the length of the specimen and the additional compressive and shear stresses during 3 PB. We estimated flexural moduli using the Classical

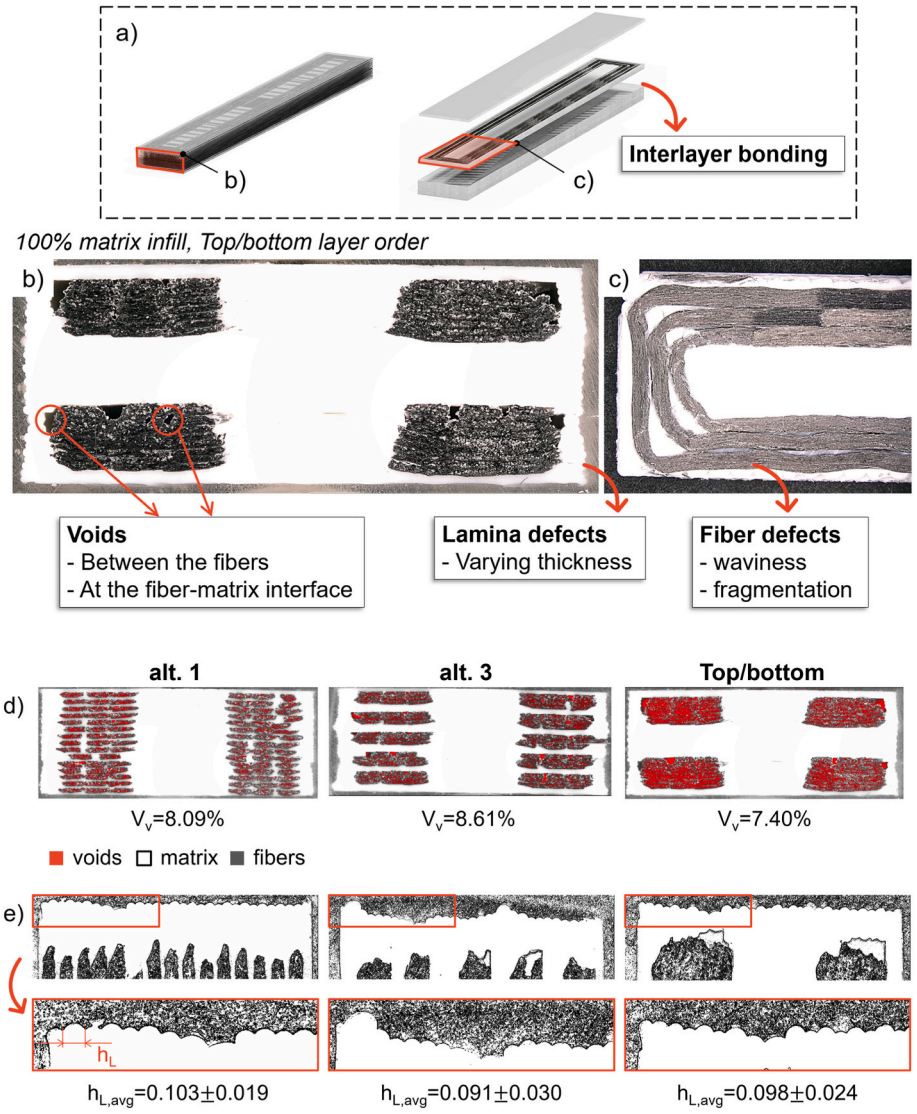

Fig. 7. Sources of defects in 3D-printed continuous fibre–reinforced composites a) interpretation of the cross-sections, b)-c) optical microscopy images to reveal the defects, d) results of the void content measurements, e) results of the lamina thickness measurements.

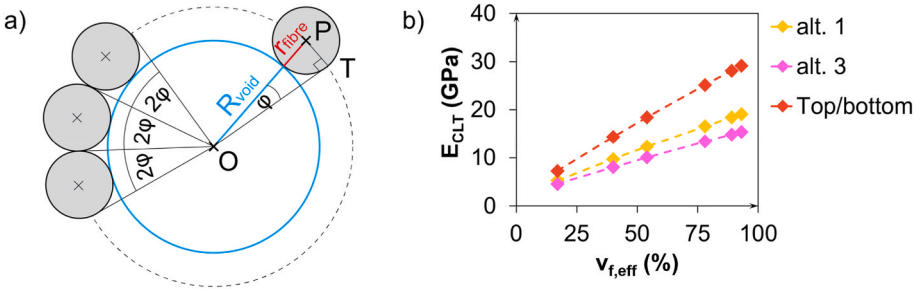

Fig. 8. a) Fibres surrounding a void b) effect of effective fibre content on the CLT-based estimated flexural modulus.

Laminate Theory (CLT), and showed that the Kerner-Hashin model can be applied to estimate the elastic properties of the matrix with voids. We examined if the boundary conditions of the model applied (CLT) are fulfilled. We used optical microscopy to show possible defects, which may cause differences between the estimated and measured moduli. Defects such as a large number of voids, non-homogeneous distribution of fibres, fibre waviness and fragmentation, and weak bonding between the laminas were identified. We also present a phenomenological analysis based on the Fibre Bundle Cell (FBC) method, which revealed the probability of failure as a function of elongation. The analysis has shown that a more gradual damage process can be achieved with the top/bottom layer order, which is more desirable for safety.

CRediT authorship contribution statement

Csenge Tóth: Writing – original draft, Visualization, Validation,

Methodology, Investigation, Conceptualization. **Ábris Dávid Virág:** Writing – original draft, Methodology, Formal analysis. **László Mihály Vas:** Writing – review & editing, Methodology, Formal analysis. **Norbert Krisztián Kovács:** Supervision, Resources, Project administration, Funding acquisition.

Declaration of competing interest

The authors declare that they have no known competing financial interests or personal relationships that could have appeared to influence the work reported in this paper.

Data availability

Data will be made available on request.

Acknowledgements

Project no. TKP-6-6/PALY-2021 has been implemented with the support provided by the Ministry of Culture and Innovation of Hungary from the National Research, Development, and Innovation Fund, financed under the TKP2021-NVA funding scheme. The research reported in this paper was supported by the National Research, Development and Innovation Office (NRDI, Hungary) through grants OTKA FK134336. The project 2022-2.1.1-NL-2022-00012 has been implemented with the support provided by the Ministry of Culture and Innovation of Hungary from the National Research, Development and Innovation Fund, financed under the 2022-2.1.1-NL Creation of National Laboratories, Complex Development funding scheme. Norbert Krisztián Kovács is thankful for the support of the ÚNKP-23-5-BME-466 New National Excellence Program of the Ministry for Culture and Innovation from the source of the National Research, Development and Innovation Fund and the János Bolyai Research Scholarship of the Hungarian Academy of Sciences. Csenge Tóth is thankful for the support of the ÚNKP-23-3-II-BME-140 supported by the New National Excellence Program of the Ministry for Culture and Innovation from the source of the National Research, Development and Innovation Fund.

Appendix

The elastic properties of a reinforced lamina were determined with the following equations [49]:

$$E_1 = E_f \nu_f + E_m(1-\nu_f) \tag{A1}$$

$$E_2 = \left[\frac{\nu_f}{E_f} + \frac{(1-\nu_f)}{E_m}\right]^{-1} \tag{A2}$$

$$G_{12} = \left[\frac{\nu_f}{G_f} + \frac{(1-\nu_f)}{G_m}\right]^{-1} \tag{A3}$$

$$\nu_{12} = \nu_f \nu_f + \nu_m(1-\nu_f) \tag{A4}$$

$$\nu_{21} = \frac{E_2}{E_1}\nu_{12} \tag{A5}$$

After the independent material properties are obtained, the reduced stiffness matrix of a lamina can be calculated as:

$$[Q_{ij}] = \begin{bmatrix} Q_{11} & Q_{12} & 0 \\ Q_{12} & Q_{22} & 0 \\ 0 & 0 & Q_{66} \end{bmatrix} \tag{A6}$$

where the terms are:

$$Q_{11} = \frac{E_{11lamina}}{1-\nu_{12lamina}\nu_{21lamina}}, Q_{12} = \frac{\nu_{12lamina}E_{11lamina}}{1-\nu_{12lamina}\nu_{21lamina}}, Q_{22} = \frac{E_{22lamina}}{1-\nu_{12lamina}\nu_{21lamina}}, Q_{66} = G_{12lamina}$$

The resulting strains can be expressed as the sum of the mid-plane strains and curvatures:

$$\begin{bmatrix} \varepsilon_{xx} \\ \varepsilon_{yy} \\ \gamma_{xy} \end{bmatrix} = \begin{bmatrix} {\varepsilon_{xx}}^0 \\ {\varepsilon_{yy}}^0 \\ {\gamma_{xy}}^0 \end{bmatrix} + z \begin{bmatrix} k_{xx} \\ k_{yy} \\ k_{xy} \end{bmatrix} \tag{A7}$$

The constitutive relation for lamina is given as follows:

$$\begin{bmatrix} \sigma_{xx} \\ \sigma_{yy} \\ \tau_{xy} \end{bmatrix} = \begin{bmatrix} \overline{Q}_{11} & \overline{Q}_{12} & 0 \\ \overline{Q}_{12} & \overline{Q}_{22} & 0 \\ 0 & 0 & \overline{Q}_{66} \end{bmatrix} \begin{bmatrix} \varepsilon_{xx} \\ \varepsilon_{yy} \\ \gamma_{xy} \end{bmatrix} \tag{A8}$$

Force and moment per unit width can be calculated as:

$$\begin{bmatrix} N_{xx} \\ N_{yy} \\ N_{xy} \end{bmatrix} = [A] \begin{bmatrix} \varepsilon^0_{xx} \\ \varepsilon^0_{yy} \\ \gamma^0_{xy} \end{bmatrix} + [B] \begin{bmatrix} k_{xx} \\ k_{yy} \\ k_{xy} \end{bmatrix}; \quad \begin{bmatrix} M_{xx} \\ M_{yy} \\ M_{xy} \end{bmatrix} = [B] \begin{bmatrix} \varepsilon^0_{xx} \\ \varepsilon^0_{yy} \\ \gamma^0_{xy} \end{bmatrix} + [D] \begin{bmatrix} k_{xx} \\ k_{yy} \\ k_{xy} \end{bmatrix} \tag{A9}$$

where:

$$[A] = \sum_{k=1}^{N} \left[\overline{Q_{ij}}\right]_k (z_k - z_{k-1}) \tag{A10}$$

$$[B] = \frac{1}{2} \sum_{k=1}^{N} \left[\overline{Q_{ij}}\right]_k \left(z_k^2 - z_{k-1}^2\right) \tag{A11}$$

$$[D] = \frac{1}{3} \sum_{k=1}^{N} \left[\overline{Q_{ij}}\right]_k \left(z_k^3 - z_{k-1}^3\right) \tag{A12}$$

Curvatures for a symmetric laminate are given as:

$$\begin{bmatrix} k_{xx} \\ k_{yy} \\ k_{xy} \end{bmatrix} = [D]^{-1} \begin{bmatrix} M_{xx} \\ M_{yy} \\ M_{xy} \end{bmatrix} \tag{A13}$$

The flexural load is applied in the z-direction. If $M_{xx} \neq 0$, $M_{yy} = 0$ and $M_{xy} = 0$, and flexural modulus along the x direction is given as:

$$E_x = \frac{12\left(D_{11}D_{22} - D_{12}^2\right)}{D_{22}h^3} \tag{A14}$$

References

[1] G.D. Goh, Y.L. Yap, S. Agarwala, W.Y. Yeong, Recent progress in additive manufacturing of fiber reinforced polymer composite, Adv. Mater. Technol. 4 (2019) 1800271, https://doi.org/10.1002/admt.201800271.

[2] S. Yuan, S. Li, J. Zhu, Y. Tang, Additive manufacturing of polymeric composites from material processing to structural design, Compos. B Eng. 219 (2021) 108903, https://doi.org/10.1016/J.COMPOSITESB.2021.108903.

[3] K. Soltanmohammadi, M. Aberoumand, D. Rahmatabadi, E. Soleyman, S. Ghasemi, I. Ghasemi, M. Baniassadi, K. Abrinia, M. Bodaghi, M. Baghani, Four-dimensional printing of acrylonitrile butadiene styrene – thermoplastic polyurethane shape memory polymers with excellent material and interfacial adhesion performance, Express Polym. Lett. 17 (2023) 1082–1095, https://doi.org/10.3144/expresspolymlett.2023.82.

[4] R.R. Fernandes, N. van de Werken, P. Koirala, T. Yap, A.Y. Tamijani, M. Tehrani, Experimental investigation of additively manufactured continuous fiber reinforced composite parts with optimized topology and fiber paths, Addit. Manuf. 44 (2021) 102056, https://doi.org/10.1016/J.ADDMA.2021.102056.

[5] V.S. Papapetrou, C. Patel, A.Y. Tamijani, Stiffness-based optimization framework for the topology and fiber paths of continuous fiber composites, Compos. B Eng. 183 (2020) 107681, https://doi.org/10.1016/J.COMPOSITESB.2019.107681.

[6] G. Liu, Y. Xiong, L. Zhou, Additive manufacturing of continuous fiber reinforced polymer composites: design opportunities and novel applications, Compos. Commun. 27 (2021) 100907, https://doi.org/10.1016/J.COCO.2021.100907.

[7] P. Cheng, Y. Peng, S. Li, Y. Rao, A. Le Duigou, K. Wang, S. Ahzi, 3D printed continuous fiber reinforced composite lightweight structures: a review and outlook, Compos. B Eng. 250 (2023), https://doi.org/10.1016/j.compositesb.2022.110450.

[8] E. Polyzos, D. Van Hemelrijck, L. Pyl, Numerical modelling of the elastic properties of 3D-printed specimens of thermoplastic matrix reinforced with continuous fibres, Compos. B Eng. 211 (2021) 108671, https://doi.org/10.1016/J.COMPOSITESB.2021.108671.

[9] M. Araya-Calvo, I. López-Gómez, N. Chamberlain-Simon, J.L. León-Salazar, T. Guillén-Girón, J.S. Corrales-Cordero, O. Sánchez-Brenes, Evaluation of compressive and flexural properties of continuous fiber fabrication additive manufacturing technology, Addit. Manuf. 22 (2018) 157–164, https://doi.org/10.1016/J.ADDMA.2018.05.007.

[10] L. Malagutti, V. Mazzanti, F. Mollica, Tensile properties of FDM 3D-printed wood flour filled polymers and mathematical modeling through classical lamination theory, Rapid Prototyp. J. 28 (2022) 1834–1842, https://doi.org/10.1108/RPJ-11-2021-0298.

[11] E. Polyzos, C. Nikolaou, D. Polyzos, D. Van Hemelrijck, L. Pyl, Direct modeling of the elastic properties of single 3D printed composite filaments using X-ray computed tomography images segmented by neural networks, Addit. Manuf. 76 (2023) 103786, https://doi.org/10.1016/J.ADDMA.2023.103786.

[12] K. Saeed, A. McIlhagger, E. Harkin-Jones, J. Kelly, E. Archer, Predication of the in-plane mechanical properties of continuous carbon fibre reinforced 3D printed polymer composites using classical laminated-plate theory, Compos. Struct. 259 (2021) 113226, https://doi.org/10.1016/J.COMPSTRUCT.2020.113226.

[13] M. Somireddy, A. Czekanski, Computational modeling of constitutive behaviour of 3D printed composite structures, J. Mater. Res. Technol. 11 (2021) 1710–1718, https://doi.org/10.1016/J.JMRT.2021.02.030.

[14] A.E. Krupnin, A.R. Zakirov, N.G. Sedush, M.M. Alexanyan, A.G. Aganesov, S. N. Chvalun, Theoretical and experimental investigation of 3D-printed polylactide laminate composites' mechanical properties, Materials 16 (2023) 7229, https://doi.org/10.3390/ma16227229.

[15] S.R. Rajpurohit, H.K. Dave, M. Bodaghi, Classical laminate theory for flexural strength prediction of FDM 3D printed PLAs, Mater. Today Proc. (2023), https://doi.org/10.1016/J.MATPR.2023.03.310.

[16] R. Torre, S. Brischetto, Experimental characterization and finite element validation of orthotropic 3D-printed polymeric parts, Int. J. Mech. Sci. 219 (2022) 107095, https://doi.org/10.1016/J.IJMECSCI.2022.107095.

[17] M. Somireddy, A. Czekanski, Anisotropic material behavior of 3D printed composite structures – material extrusion additive manufacturing, Mater. Des. 195 (2020) 108953, https://doi.org/10.1016/J.MATDES.2020.108953.

[18] S. Li, P. Cheng, S. Ahzi, Y. Peng, K. Wang, F. Chinesta, J.P.M. Correia, Advances in hybrid fibers reinforced polymer-based composites prepared by FDM: a review on mechanical properties and prospects, Compos. Commun. 40 (2023), https://doi.org/10.1016/j.coco.2023.101592.

[19] T. Li, L. Wang, Bending behavior of sandwich composite structures with tunable 3D-printed core materials, Compos. Struct. 175 (2017) 46–57, https://doi.org/10.1016/J.COMPSTRUCT.2017.05.001.

[20] A. Montazeri, E. Bahmanpour, M. Safarabadi, Three-point bending behavior of foam-filled conventional and auxetic 3D-printed honeycombs, Adv. Eng. Mater. 25 (2023), https://doi.org/10.1002/adem.202300273.

[21] M. Zahed, R. Ardeshiri Jouneghani, M. Safarabadi, Reinforcement of 3D-printed Re-entrant structures using additional supports under three-point bending, experimental and numerical analyses, Adv. Eng. Mater. 26 (2024), https://doi.org/10.1002/adem.202301252.

[22] A. Montazeri, A. Hasani, M. Safarabadi, Bending performance and failure mechanism of 3D-printed hybrid geometry honeycombs with various Poisson's ratios, J. Sandw. Struct. Mater. 25 (2023) 709–729, https://doi.org/10.1177/10996362231194713.

[23] A. Montazeri, E. Bahmanpour, M. Safarabadi, A Poisson's ratio sign-switching mechanical metamaterial with tunable stiffness, Int. J. Mech. Sci. 260 (2023), https://doi.org/10.1016/j.ijmecsci.2023.108670.

[24] A. Montazeri, A. Saeedi, E. Bahmanpour, M. Safarabadi, Enhancing the compressive properties of re-entrant honeycombs by line defects with insight from nature, Mater. Today Commun. 38 (2024), https://doi.org/10.1016/j.mtcomm.2023.107700.

[25] C. Huang, M.W. Joosten, 3D printed continuous fibre-reinforced composites: design and characterisation of advanced pseudo-ductile hybrid laminates, Composer Part A Appl Sci Manuf 146 (2021), https://doi.org/10.1016/j.compositesa.2021.106403.

[26] J. Shang, W. Zhang, F. Liu, S. Wang, M. Tian, X. Ding, Z-direction performance and failure behavior of 3D printed continuous fiber reinforced composites with sinusoidal structure, Compos. Sci. Technol. 239 (2023), https://doi.org/10.1016/j.compscitech.2023.110069.

[27] L. Ma, K. Zhang, Z. Pan, W. Zhou, J. Liu, Experimental investigation on the mechanical behavior and damage of 3D printed composites under three-point bending, J. Compos. Mater. 56 (2022) 1019–1037, https://doi.org/10.1177/00219983211066389.

[28] Z. Hou, X. Tian, J. Zhang, L. Zhe, Z. Zheng, D. Li, A.V. Malakhov, A.N. Polilov, Design and 3D printing of continuous fiber reinforced heterogeneous composites, Compos. Struct. 237 (2020) 111945, https://doi.org/10.1016/J.COMPSTRUCT.2020.111945.

[29] L. Mészáros, A. Horváth, L.M. Vas, R. Petrény, Investigation of the correlations between the microstructure and the tensile properties multi-scale composites with a polylactic acid matrix, reinforced with carbon nanotubes and carbon fibers, with the use of the fiber bundle cell theory, Compos. Sci. Technol. 242 (2023) 110154, https://doi.org/10.1016/J.COMPSCITECH.2023.110154.

[30] L.M. Vas, Z. Rácz, Modeling and testing the fracture process of impregnated carbon-fiber roving specimens during bending: Part I – fiber bundle model,

J. Compos. Mater. 38 (2004) 1757–1785, https://doi.org/10.1177/0021998304044767.
[31] L.M. Vas, P. Tamás, E. Bognár, P. Nagy, R. Késmárszky, K. Pap, G. Szebényi, Nonlinear fiber-bundle-cells-based phenomenological modeling of human tissue samples, Biomech. Model. Mechanobiol. 21 (2022) 1803–1823, https://doi.org/10.1007/s10237-022-01621-1.
[32] A. Parmiggiani, M. Prato, M. Pizzorni, Effect of the fiber orientation on the tensile and flexural behavior of continuous carbon fiber composites made via fused filament fabrication, Int. J. Adv. Des. Manuf. Technol. 114 (2021) 2085–2101, https://doi.org/10.1007/s00170-021-06997-5.
[33] F. Korkees, J. Allenby, P. Dorrington, 3D printing of composites: design parameters and flexural performance, Rapid Prototyp. J. 26 (2020) 699–706, https://doi.org/10.1108/RPJ-07-2019-0188.
[34] V. Cojocaru, D. Frunzaverde, C.O. Miclosina, On the behavior of honeycomb, grid and triangular PLA structures under symmetric and asymmetric bending, Micromachines 14 (2023), https://doi.org/10.3390/mi14010120.
[35] B. Aloyaydi, S. Sivasankaran, A. Mustafa, Investigation of infill-patterns on mechanical response of 3D printed poly-lactic-acid, Polym. Test. 87 (2020) 106557, https://doi.org/10.1016/J.POLYMERTESTING.2020.106557.
[36] Markforged material datasheet, (https://web-objects.markforged.com/craft/materials/CompositesV5.2.pdf) (Accessed 10 April 2024).
[37] H. Zhang, J. Chen, D. Yang, Fibre misalignment and breakage in 3D printing of continuous carbon fibre reinforced thermoplastic composites, Addit. Manuf. 38 (2021), https://doi.org/10.1016/j.addma.2020.101775.
[38] R.R. Fernandes, A.Y. Tamijani, M. Al-Haik, Mechanical characterization of additively manufactured fiber-reinforced composites, Aero. Sci. Technol. 113 (2021) 106653, https://doi.org/10.1016/J.AST.2021.106653.
[39] J.M. Chacón, M.A. Caminero, P.J. Núñez, E. García-Plaza, I. García-Moreno, J. M. Reverte, Additive manufacturing of continuous fibre reinforced thermoplastic composites using fused deposition modelling: effect of process parameters on mechanical properties, Compos. Sci. Technol. 181 (2019), https://doi.org/10.1016/j.compscitech.2019.107688.
[40] S. Yu, Y.H. Hwang, J.Y. Hwang, S.H. Hong, Analytical study on the 3D-printed structure and mechanical properties of basalt fiber-reinforced PLA composites using X-ray microscopy, Compos. Sci. Technol. 175 (2019) 18–27, https://doi.org/10.1016/j.compscitech.2019.03.005.
[41] M. Galati, M. Viccica, P. Minetola, A finite element approach for the prediction of the mechanical behaviour of layered composites produced by Continuous Filament Fabrication (CFF), Polym. Test. 98 (2021) 107181, https://doi.org/10.1016/J.POLYMERTESTING.2021.107181.
[42] M. Jalalvand, G. Czél, M.R. Wisnom, Damage analysis of pseudo-ductile thin-ply UD hybrid composites – a new analytical method, Composer Part A Appl Sci Manuf 69 (2015) 83–93, https://doi.org/10.1016/J.COMPOSITESA.2014.11.006.
[43] M.M. Shokrieh, S.M. Kamali Shahri, Modeling Residual Stresses in Composite Materials, Residual Stresses in Composite Materials, 2021, pp. 193–213, https://doi.org/10.1016/B978-0-12-818817-0.00006-8.
[44] P. Kumar Mishra S P, Prediction of in-plane stiffness of multi-material 3D printed laminate parts fabricated by FDM process using CLT and its mechanical behaviour under tensile load, Mater. Today Commun. 23 (2020) 100955, https://doi.org/10.1016/J.MTCOMM.2020.100955.
[45] M. Meng, H.R. Le, M.J. Rizvi, S.M. Grove, 3D FEA modelling of laminated composites in bending and their failure mechanisms, Compos. Struct. 119 (2015) 693–708, https://doi.org/10.1016/J.COMPSTRUCT.2014.09.048.
[46] H. Shiratori, A. Todoroki, M. Ueda, R. Matsuzaki, Y. Hirano, Mechanism of folding a fiber bundle in the curved section of 3D printed carbon fiber reinforced plastics, Adv. Compos. Mater. 29 (2020) 247–257, https://doi.org/10.1080/09243046.2019.1682794.
[47] C. Pascual-González, P. San Martín, I. Lizarralde, A. Fernández, A. León, C.S. Lopes, J.P. Fernández-Blázquez, Post-processing effects on microstructure, interlaminar and thermal properties of 3D printed continuous carbon fibre composites, Compos. B Eng. 210 (2021) 108652, https://doi.org/10.1016/J.COMPOSITESB.2021.108652.
[48] M. Iragi, C. Pascual-González, A. Esnaola, C.S. Lopes, L. Aretxabaleta, Ply and interlaminar behaviours of 3D printed continuous carbon fibre-reinforced thermoplastic laminates; effects of processing conditions and microstructure, Addit. Manuf. 30 (2019) 100884, https://doi.org/10.1016/J.ADDMA.2019.100884.
[49] E.J. Barbero, Introduction to Composite Materials Design, third ed.), third ed., CRC Press., Boca Raton, 2017.